Plane-wave fluorescence tomography with adaptive finite elements

Amit Joshi

Photon Migration Laboratories, Department of Radiology, Baylor College of Medicine, Houston, Texas 77030

Wolfgang Bangerth

Department of Mathematics, Texas A & M University, College Station, Texas 77840

Kildong Hwang, John Rasmussen, and Eva M. Sevick-Muraca

Photon Migration Laboratories, Department of Radiology, Baylor College of Medicine, Houston, Texas 77030

Received July 28, 2005; revised October 5, 2005; accepted October 11, 2005

We present three-dimensional fluorescence yield tomography of a tissue phantom in a noncontact reflectance imaging setup. The method employs planar illumination with modulated light and frequency domain fluorescence measurements made on the illumination plane. An adaptive finite-element algorithm is used to handle the ill-posed and computationally demanding inverse image reconstruction problem. Tomographic images of fluorescent targets buried at 1–2 cm depths from the illumination surface demonstrate the feasibility of fluorescence tomography from reflectance tomography in clinically relevant tissue volumes.

OCIS codes: 110.3080, 170.5280, 170.6960.

Future advancements in molecular medicine depend to a great degree on the *in vivo* detection of molecular processes that precede disease symptoms. Thus fluorescence optical tomography holds great promise by virtue of its ability to target contrast in deep subsurface tissues by using imaging agents such as bioconjugated fluorescent dyes[1] or quantum dots.[2] Traditional approaches to fluorescence optical tomography in clinically relevant volumes have utilized fiber-optic-based source–detector arrays wherein both the reflectance and the transmittance measurements are acquired.[3] However, in clinical applications such as sentinel lymph node mapping for diagnosis and staging of breast cancer or melanoma, transmittance measurements of fluorescence photon migration are not possible. Furthermore, fiber-optic-based source–detector arrays sample the measurement space only sparsely, thus increasing the ill-posedness of the image reconstruction problem. On the other hand, area-illumination and area-detection fluorescence tomography schemes allow the acquisition of a dense set of fluorescence measurements in a noncontact fashion,[4] though such schemes involve the additional complexity of characterizing the excitation source pattern[5] and the availability of only one projection for image reconstruction. To circumvent the latter problem, time-dependent or photon migration measurements are necessary to obtain three-dimensional reconstructions of fluorescence distribution from two-dimensional surface measurements. To reduce computational requirements, adaptive discretizations can be used to capture the variation of the surface excitation pattern as well as to resolve the fluorescence yield map; this contrasts with the traditional use of *a priori* discretizations of the fluorescence yield map. Adaptive finite-element approaches have been demonstrated successfully in other fields; in these methods the meshes are locally and automatically refined to capture variations of the discretized field. Besides affecting the tomographic image resolution, adaptive discretization approaches enable computationally efficient and rapid solution of the image reconstruction problem. Previously we reported a novel tomography algorithm for reconstructing three-dimensional fluorescence yield maps from simulated two-dimensional area-illumination and area-detection measurements.[6] Here we report the results of fluorescence tomography from experimentally obtained frequency domain fluorescence measurements on a tissue phantom with buried fluorescent targets at depths of 1 and 2 cm beneath the illumination surface.

Figure 1 illustrates the tissue phantom with embedded fluorescent targets interrogated by use of a gain-modulated image-intensified CCD camera system.[3,5] The tissue phantom consisted of a clear 512 cm^3 acrylic box filled with 1% Liposyn solution (v/v water) and held a fluorescent target consisting of a 0.5 cm diameter glass bulb filled with 1 μM Indocyanine Green (ICG) dye solution in 1% Liposyn. The tissue phantom was illuminated on the top surface with an expanded beam from a 785 nm laser diode modulated at 100 MHz. The florescence image of the surface was isolated from the excitation image through a 785 nm holographic band-rejection filter and an 830 nm bandpass filter. The fluorescence amplitude and phase images were obtained by using the homodyne technique.[5] Since model-based tomographic reconstructiion requires accurate excitation source information, the singly scattered excitation light was characterized and taken to be representative of the incident excitation. This singly scattered excitation component was isolated by using cross polarizers.[5,7]

The fluorescence image reconstruction problem was posed as a constrained optimization problem wherein an L_2 norm-based error functional of the distance between boundary fluorescence measurements

0146-9592/06/020193-3/$15.00

and the diffusion model predictions was minimized with the constraint that the coupled diffusion model be satisfied. In a function space setting this minimization problem reads as

$$\min_{q,u,v} J(q,v) \quad \text{subject to} \quad A(q;[u,v])([\zeta,\xi]) = 0. \tag{1}$$

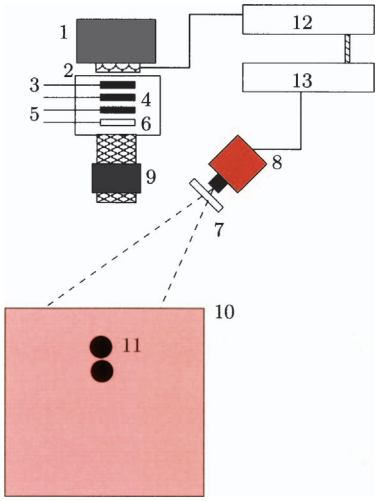

Fig. 1. ICCD detection system. 1, CCD camera; 2, image intensifier; 3, 4, 5, optical filters; 6, 7, linear polarizers; 8, 785 nm laser diode; 9, 80–200 mm zoom lens; 10, tissue phantom; 11, fluorescent targets; 12, 13, phase-locked oscillators.

Here the error functional $J(q,v)$ incorporates a least-squares error term over the measurement region Σ and a Tikhonov regularization term:

$$J(q,v) = (1/2)\|v - \sigma z\|_{\Sigma}^2 + \beta r(q), \tag{2}$$

where $[u,v]$ represent the excitation and emission fluences, $q=\mu_{axf}$ denotes the unknown fluorescence map, and σ is a scaling factor accounting for the unknown excitation strength. The constraint $A(q;[u,v])([\zeta,\xi])=0$ is the weak form of the well-known coupled photon diffusion equations in the frequency domain with partial current boundary conditions and with test functions $[\zeta,\xi] \in H^1(\Omega)$. It is obtained from the photon diffusion equations by multiplication by test functions $[\zeta,\xi]$ and integration over the domain Ω; a more detailed discussion as well as these equations can be found elsewhere.[6] The semilinear form so derived is defined as

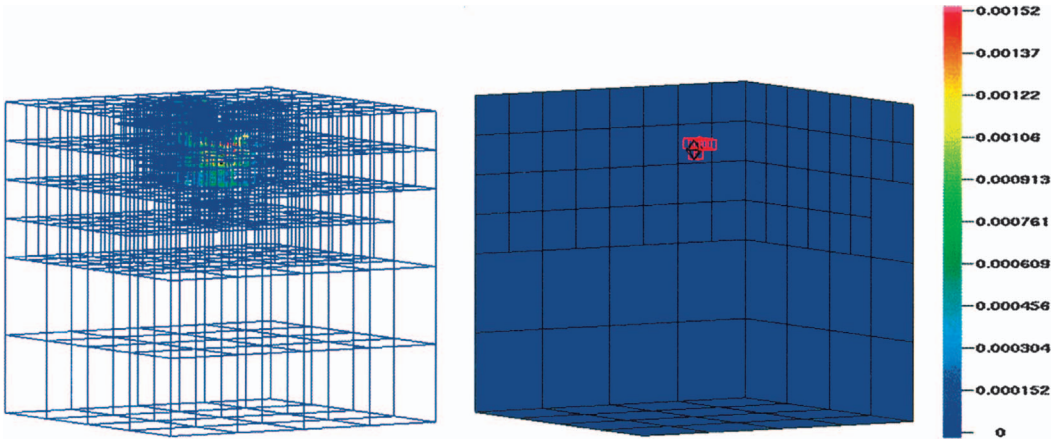

Fig. 2. Reconstructed image (right) and the final fluorescence absorption map laid over the computational grid (left) for the 1 cm deep target. The top 10% of the contour levels of the μ_{axf} map are depicted. The black wireframe sphere in the right-hand image depicts the true target location, and the red blocks identify the recovered target.

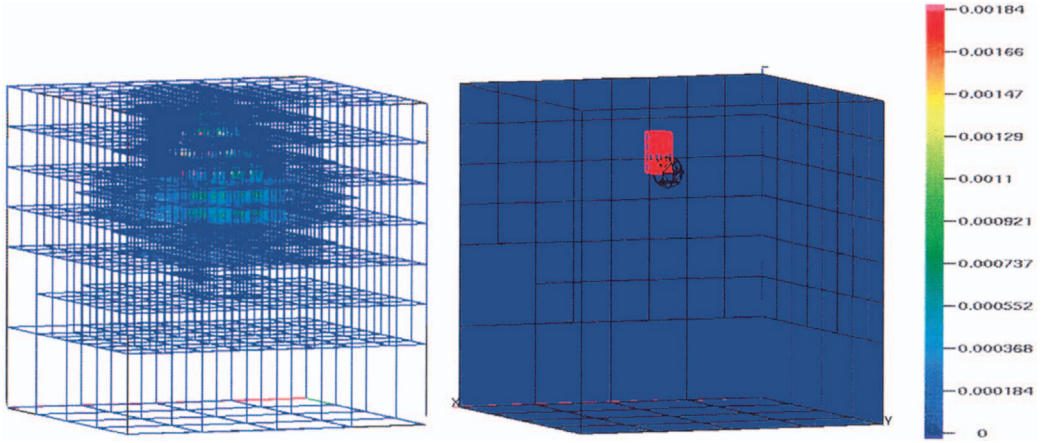

Fig. 3. Reconstructed image (right) and the final fluorescence absorption map laid over the computational grid (left) for the 2 cm deep target. The top 10% of the contour levels of the μ_{axf} map are depicted. The black wireframe sphere in the right-hand image depicts the true target location, and the red blocks identify the recovered target.

$$A(q;[u,v])([\zeta,\xi]) = (D_x \nabla u, \nabla\zeta)_\Omega + (k_x u, \zeta)_\Omega + \frac{\gamma}{2}(u,\zeta)_{\partial\Omega} + \frac{1}{2}(S,\zeta)_{\partial\Omega} + (D_m \nabla v, \nabla\xi)_\Omega + (k_m v, \xi)_\Omega + \frac{\gamma}{2}(v,\xi)_{\partial\Omega} - (\beta_{xm} u, \xi)_\Omega. \quad (3)$$

Here $D_{x,m}$ denotes the diffusion coefficients at excitation and emission wavelengths; $k_{x,m}$ denotes the attenuation terms, which depend on the absorption due to endogenous chromophores and absorption due to exogenous fluorophores; and β_{xm} is the coupling term for excitation and emission equations. β_{xm} depends on the fluorophore quantum efficiency, lifetime, and absorption due to the fluorophore at the excitation wavelength. The constrained optimization problem (1) is solved by introducing a Lagrangian functional:

$$L([u,v],[\lambda^{ex},\lambda^{em},q]) = J(q,v) + A(q;[u,v])([\lambda^{ex},\lambda^{em}]). \quad (4)$$

Here $\lambda^{ex},\lambda^{em}$ are the Lagrange multipliers corresponding to the excitation and the emission diffusion equation constraints, respectively. A stationary point of the Lagrangian is sought by using the Gauss–Newton method. For actual computations, we discretized the Gauss–Newton equations with the finite-element method. State and adjoint variables u, v, λ^{ex}, and λ^{em} were discretized and solved on a mesh with continuous finite elements (termed the state mesh), while the unknown parameter map q is discretized on a separate mesh with discontinuous finite elements (termed the parameter mesh).

Whenever Gauss–Newton iterations on these meshes reduced the error function by a significant amount, both meshes were refined by using an *a posteriori* refinement criteria. These criteria compute, for each finite-element cell, an indicator of the error associated with this cell. A certain fraction of the cells with the largest indicator values are then subdivided into smaller cells for better resolution, while the cells with the lowest indicators are coarsened.[6] The choice of two separate meshes means that the state mesh can be fine close to the source, where the excitation fluence greatly varies, while the parameter mesh will be fine only close to the fluorescent target and coarse everywhere else. This scheme was implemented in a program based on the deal.II library.[8]

Figures 2 and 3 depict the reconstructed images of the 1 and 2 cm deep fluorescent targets. The image reconstruction procedure was initiated with coarse state ($8\times8\times8=512$ cells) and parameter ($4\times4\times4=64$ cells) meshes. Computations were performed on a 2 GHz Pentium-M notebook computer with 2 Gbytes of memory. Image reconstructions required 12–15 min of computational time, depending on the target depth. The top 10% of the contour levels of the reconstructed fluorescence absorption were considered to constitute the fluorescent heterogeneity. Both state and parameter meshes were automatically refined during reconstruction. The state mesh was predominantly refined at the illumination surface to accurately resolve the incident excitation illumination; the parameter mesh was fine mainly in the region containing the recovered fluorescent target. Four automatic mesh refinements were triggered.

Table 1. Summary of Reconstructed Images

Image Attributes	Target Depth: 1 cm	Target Depth: 2 cm
True centroid (cm)	4.0, 4.0, 6.75	4.0, 3.8, 5.75
Recovered centroid (cm)	4.0, 4.0, 6.8	4.2, 3.7, 6.25
True volume (cm^3)	0.0654	0.0654
Recovered volume (cm^3)	0.0938	0.25

These reconstructions are summarized in Table 1. The minimum mesh size of the final parameter mesh was 1.25 mm (for a graphical depiction of the meshes, see Figs. 2 and 3). To obtain the same level of resolution on a globally refined mesh, 262,144 cells would be required. On the other hand, with the adaptive refinement, this resolution was achieved with only 2584 cells for the 1 cm deep target and 2416 cells for the 2 cm deep target. The recovered target for the 2 cm target depth was shifted toward the illumination surface, and the recovered volume was enlarged. This may be attributed to the lower fluorescence signal penetrating up to the measurement surface, which was corrupted to a greater degree by the excitation light leakage through the fluorescence filters than the fluorescence signal arising from the 1 cm deep target.[9] The slight lateral displacement of the recovered targets may also be due to the uncertainty in target positioning as well as to the fact that the excitation source was not laterally symmetric with respect to the position of fluorescent target.

In this Letter we have demonstrated what we believe to be the first ever adaptive finite-element-based reconstructions from experimentally obtained frequency domain fluorescence measurements on a clinically relevant tissue phantom.

References

1. R. Weissleder, C.-H. Tung, U. Mahmood, and A. Bogdanov, Nat. Biotechnol. **21**, 375 (1999).
2. S. Kim, Y. Lim, E. Soltesz, J. L. A. M. De Grand, A. Nakayama, J. A. Parker, T. Mihaljevic, R. G. Laurence, D. M. Dor, L. H. Cohn, M. G. Bawendi, and J. Frangioni, Nat. Biotechnol. **22**, 93 (2004).
3. A. Godavarty, M. J. Eppstein, C. Zhang, S. Theru, A. B. Thompson, M. Gurfinkel, and E. M. Sevick-Muraca, Phys. Med. Biol. **48**, 1701 (2003).
4. R. Roy, A. Thompson, A. Godavarty, and E. M. Sevick-Muraca, IEEE Trans. Med. Imaging **24**, 137 (2005).
5. A. B. Thompson and E. M. Sevick-Muraca, J. Biomed. Opt. **8**, 111 (2002).
6. A. Joshi, W. Bangerth, and E. M. Sevick-Muraca, Opt. Express **12**, 5402 (2004).
7. S. L. Jacques, J. R. Roman, and K. Lee, Lasers Surg. Med. **26**, 119 (2000).
8. W. Bangerth, R. Hartmann, and G. Kanschat, "deal.II: a finite element differential equations analysis library" (2005), http://www.dealii.org/.
9. K. Hwang, J. Houston, J. Rasmussen, A. Joshi, S. Ke, C. Li, and E. Sevick-Muraca, J. Mol. Imaging **4**, 194 (2005).